Desalination and Water Treatment
www.deswater.com

doi: 10.5004/dwt.2022.28412

258 (2022) 179–189
May

Structure and photocatalytic activity of porous g-C_3N_4 and Cu_2O@g-C_3N_4 system toward Rhodamine B degradation under solar light irradiation

R.M. Basal*, H.A. Kiwaan, M.R. Mostafa

Chemistry Department, Faculty of Science, Damietta University, Damietta 34517, Egypt, emails: rahmamohammed133@gmail.com/rahmabasl@du.edu.eg (R.M. Basal), hkiwaan@gmail.com/hkiwaan@mans.edu.eg (H.A. Kiwaan), ramzy1950@gmail.com/ramzy1950@mans.edu.eg (M.R. Mostafa)

Received 8 December 2021; Accepted 16 March 2022

ABSTRACT

Bulk g-C_3N_4 (CNI) was prepared via direct pyrolysis of urea at 550°C. Two porous g-C_3N_4 materials (CNII and CNIII) were synthesized using silica nanoparticles template obtained via two different routes with keeping the mass ratio of urea to silica constant at (1:1). CNIII sample was load with different amounts of CuO to prepare Cu_2O@CNIII photocatalysts. The synthesized materials were characterized by X-ray diffraction, scanning electron microscopy, Fourier-transform infrared spectroscopy, N_2 adsorption–desorption measurements, ultraviolet-visible spectroscopy (UV-Vis), and X-ray photoelectron spectroscopy. N_2 adsorption–desorption measurements showed that the porous structure of CNII and CNIII has a huge surface area (50.4–85.2 m^2/g) than that of bulk g-C_3N_4 (CNI). The surface area of CNIII samples decreased with the increase of Cu_2O content in Cu_2O@CNIII materials. The data obtained from the photocatalytic degradation of Rhodamine B (RhB) dye reveal that the addition of Cu_2O to CNIII increased the photocatalytic activity when compared to CNI, CNII and metal free-CNIII photocatalysts. The high activity of CNII and CNIII samples was attributed to the texture properties while that for Cu_2O@CNIII samples was related to the synergetic effect of both surface area and the presence of Cu_2O nanoparticles. The experimental data was explained in terms of pseudo-first-order kinetics model. The recyclability study reveals that the investigated photocatalysts were highly stable and can be reused for up to four successful runs without a major loss in their activity. From free radical trapping studies, the major reactive species photoinduced holes and super oxide radicals play an important role in the degradation of RhB.

Keywords: Photocatalytic degradation; Rhodamine B; Porous carbon nitride; Cu_2O@porous carbon nitride; Kinetics

1. Introduction

Numerous industrial processes such as clothing, leather tanning, food, hair coloring and paper industries represent the main sources of dyes in wastewater. About 15% of the dyes used in these processes are non-biodegradable and discharged into water bodies and natural streams [1–3]. Majority of these dyes are poisonous and carcinogenic thus causing impair the environment and human health [4], therefore the disposal of effluents containing these pollutants needs a previous suitable treatment technique to reduce their potential magnified impacts on environment. Many technologies have been used to treat textile industry effluents such as adsorption [5,6], photodegradation [7–9], biological process [10,11], electrochemical [12,13] and advanced oxidation process (AOPs) [14,15]. Among the processes which have been used to minimize dyes concentrations in surface and wastewater to acceptable levels, photocatalysis degradation process represents an efficient and economical tool. It employs light radiation in the presence of a

---

* Corresponding author.

photocatalyst to accelerate the degradation of dye molecules to some nontoxic stable products such as CO_2 and H_2O [16–18]. This tool has many advantages, for instance, simple operation conditions, stability, low costs and toxicity, hydrophilicity, and availability [19–21].

Several attempts have been made in the last decade to identify visible-light driven photocatalysts for the degradation of organic contaminants. Carbon nitride (g-C_3N_4) has received a lot of interest in this area. A large variety of abundant nitrogen rich precursors such as urea, thiourea, melamine, cyanamide, and dicyanamide are used to synthesized g-C_3N_4 [22,23]. However bulk g-C_3N_4 synthesized from these materials showed low visible-light absorption capacity [24] and insufficient surface-active sites [25] which leads to the rapid recombination of photoinduced electron–hole pairs [26]. Therefore, numerous attempts have been made to modify the chemical structure and the surface properties of g-C_3N_4 including surface active sites and their porous structure. Among the various structural modification techniques, doping of bulk g-C_3N_4 with metals or non-metals materials creating different g-C_3N_4 nanostructures with varying morphologies and porosity which leads to increase their surface area, enlarging visible-light harvesting ability, and reduced photogenerated electron–hole pair recombination [27,28]. Immobilization of noble metals such as Pd, Au, and Pt into g-C_3N_4 [29–31] has been employed in this regard to increase charge separation by trapping photogenerated electrons and inhibiting their interaction with holes. In recent years, great interest has focused on combining g-C_3N_4 with the oxides of non-noble metals such as ZnO [32], NiO [33], CuO [34,35], and WO_3 [36] to produce low-cost hybrid materials to decompose a wide range of organic pollutants, such as dyes.

In the present work, bulk g-C_3N_4 (CNI) was obtained by pyrolyzing urea directly at 550°C. Two porous g-C_3N_4 materials have been prepared by using urea and SiO_2 as template through two different routes with keeping the mass ratio of urea to silica content at 1:1. One route (A) to obtain porous g-C_3N_4 (CNII) used synthesized colloidal silica with average pore diameter 50 nm as prepared and reported by Moller et al. [3]. In another route (B) the silica template was produced in a one-pot sol-gel process by mixing urea and the required amount of tetraethyl orthosilicate followed by thermal condensation of the product [38] the sample was denoted as CNIII. To prepare Cu_2O@CNIII photocatalysts, CNIII material was loaded with different amounts of Cu_2O. The photocatalysts were characterized by several techniques and their photocatalytic activities toward the degradation of Rhodamine B (RhB) under solar light irradiation were investigated.

2. Experimental

2.1. Chemicals used

Urea, tetraethyl orthosilicate (TEOS), cetyltrimethyl ammonium bromide (CTAB), triethanolamine (TEA), ethanol (C_2H_5OH), copper(II) nitrate hemi-pentahydrate ($Cu(NO_3)_2{\cdot}2.5H_2O$) and sodium borohydride ($NaBH_4$) were supplied from Sigma-Aldrich and employed as received without further treatment. Deionized water (DI H_2O) was used throughout the experiments.

2.2. Synthesis of bulk g-C_3N_4 (CNI sample)

Bulk graphitic carbon nitride, g-C_3N_4 (CNI sample) was obtained via direct pyrolysis of urea. Typically, 5 g of urea was dissolved in 10 mL of DI H_2O and then dried over water bath at 75°C for 12 h. The dried material was put in a covered crucible and placed in a muffle furnace and heated at 550°C for 4 h with the ramping rate of 5°C/min. The pale-yellow product was ground and kept for further use.

2.3. Route A: synthesis of CNII sample

Firstly colloidal silica was obtained according procedure B reported by Moeller et al. [37], typically 18.5 mL of TEOS and 98.6 mmol of TEA were mixed in a beaker and heated at 85°C for 30 min without stirring. This mixture was added dropwise to a solution containing 1.34 mole DI H_2O and 2.17 mmol CTAB preheated to 65°C. The whole solution was stirred for 2 h and leave to cool to room temperature. A white solution was obtained, and the pH of the solution was found to be 9.3. Finally, CTAB was extracted by using 2 wt.% NH_4NO_3/ethyl alcohol solution. The colloidal silica obtained was used as a hard template to prepare CNII sample as follows: 10 g of urea was dissolved in 15 mL of DI water and then this solution was added slowly to the colloidal silica solution and the mixture was kept overnight on a water bath until drying. The remaining precipitable was transferred to a crucible and heated at 550°C for 4 h with a ramping rate 5°C/min. To remove the silica template from the resulting yellow solid, the product was treated with 2N HF solution for 24 h at room temperature. The solid obtained was washed several times by DI H_2O then with ethanol and dried at 70°C for 4 h.

2.4. Route B: synthesis of CNIII sample

An alternative porous g-C_3N_4 (CNIII sample) was synthesized by using sol-gel/thermal/condensation technique [38]. Briefly 5 g of urea was dissolved 20 mL of DI H_2O and 30 mL of ethanol and the pH of the solution is adjusted to 1.8 by the addition of 0.5 N HCl. To the above solution 18.5 mL of TEOS was added drop-wise under stirring, the mixture was further stirred for 30 min at room temperature. After removing the solvents by heating the mixture at 75°C for 12 h, the solid was heated to 550°C with a ramping rate 5°C/min and kept at this temperature for 4 h. The solid is treated with 2 N HF solution for 24 h to remove SiO_2 and subsequent washed with DI H_2O and then with ethanol and finally dried at 70°C for 4 h.

2.5. Synthesis of Cu_2O@CNIII samples

Firstly, CuO sample was obtained by annealing $Cu(NO_3)_2{\cdot}2.5H_2O$ at 400°C for 6 h. CuO@CNIII samples were synthesized by a simple impregnation method. Typically, 10 mL of DI H_2O containing the appropriate amount of copper nitrate was taken in a 25 mL beaker and then a fixed amount of CNIII was dispersed using a sonicator. The above mixture was maintained at 70°C for 8 h to ensure the evaporation of the solvent. Four different CuO@CNIII photocatalysts containing 1, 2, 5 and 7 wt.% CuO were obtained and labeled as 1CNIII, 2CNIII, 5CNIII and 7CNIII, respectively. The samples were calcined at 350°C for 6 h. Each of the above solids was dispersed in 40 mL DI H_2O followed by the slowly addition of 100 mg of $NaBH_4$ which acts as reducing agent. Each mixture was stirred at room temperature for 4 h. and the solid sample was separated by centrifugation and washed several times by DI H_2O then by ethanol and finally dried at 70°C overnight.

2.6. Samples characterization

X-ray diffraction (XRD) patterns of some selected samples were obtained on Shimadzu XRD 6000 diffractometer equipped with nickel filtered Cu K_α source operated at 40 KV, 30 mA and the patterns were recorded in the 2θ range of 10°–80°. Surface morphology of the photocatalysts was studied, by the help of scanning electron microscopy (SEM) on JEOL, JSM-6510 LV. The functional groups characterized the surface of the tested samples were examined by recording their Fourier-transform infrared (FT-IR) spectra on a JASCO infrared spectrometer (Model 4100). Textural properties (surface area and pore size) were estimated from nitrogen adsorption–desorption isotherms measured at 77 K using Quanta-chrome Nova, model 3200. The surface area was calculated by using BET equation [39] while the pore size distribution was obtained from BJH method [40]. The UV-visible diffuse reflectance spectra (UV-Vis DRS) in the range 260–800 nm were recorded using Lambda AAS 800 spectrophotometer (Perkin-Elmer, USA). The chemical state of different elements of each photocatalyst was analyzed using X-ray photoelectron spectrometer (XPS) (Thermo Fisher Scientific, USA).

2.7. Photocatalytic process

All experiments have been carried out in a mechanically stirred jacketed Pyrex beaker of volume 500 mL at room temperature. Initially, 300 mg of the photocatalysts was added to 100 mL of RhB dye at a concentration of 15 mg/L. To achieve the sorption balance between RhB solution and the photocatalyst, the photocatalyst solution was kept in the dark for 60 min. After that the mixture was subjected to sunlight, under similar conditions between 10 AM to 1.0 PM. The intensity of sunlight during this time period was nearly constant as measured by oxalic acid/uranyl sulfate method. At different interval times, 2 mL of the suspension was taken and then centrifuged to remove photocatalyst particles and the remaining concentration of RhB in the supernatant was measured at λ_{max} = 545 nm using UV-Vis spectrophotometer. The photocatalytic degradation of RhB over the tested samples is expressed by $[RhB]_t/[RhB]_0$ where $[RhB]_t$ is the remaining concentration of RhB at time t and $[RhB]_0$ is the primary concentration of RhB dye. To estimate the active species during the photocatalytic degradation of RhB a series of scavengers were added to the reaction medium. Benzoquinone (BQ) and iso-propanol (IPA) were used to scavenge $O_2^{\bullet-}$ and $OH^\bullet$ radicals while potassium iodide (KI) and silver nitrate was added to scavenge holes and electrons, respectively.

3. Results and discussion

3.1. Structure characterization

Fig. 1 illustrates the wide angle XRD patterns of bulk g-C_3N_4 (CNI) and two metal free-porous C_3N_4 samples synthesized via two different routes (CNII and CNIII). As indicated from Fig. 1 distinct diffraction lines are observed at 2θ = 13.1° and 27.4° for all samples. The strong diffraction line located at 27.4° corresponding to the (002) plane which is a characteristic of inter-planer stacking diffraction line of conjugated aromatic system. The weak diffraction line located around 13.1° corresponding to the (100) plane which is a signed to an in-planer structural packing motif of tri-s-triazine units. In the case of bulk g-C_3N_4 obtained from direct pyrolysis of urea (CNI) both (100) and (002) diffraction lines [41] are more intense than the other two samples (CNII and CNIII), indicating that the crystal growth of g-C_3N_4 is inhibited by utilization of SiO_2 as a hard template.

Fig. 1 included also the XRD patterns of 5CNIII as a representative sample. As observed from Fig. 1, the patterns of this sample did not exhibit any diffraction lines corresponding to the presence of Cu_2O phase. It seems that to identify a metal oxide component by XRD it should be exceed to a certain ratio of the total composition. The results also confirmed that with increasing Cu_2O content the intensity of the diffraction lines located at 13.1° and 27.4° decreased indicating that the presence of Cu_2O inhibited the crystallinity of CNIII sample.

The microstructure and the surface morphology of CNI, CNII, CNIII and the sample containing 5 wt.% Cu_2O (5CNIII) were inspected through SEM as indicated in Fig. 2.

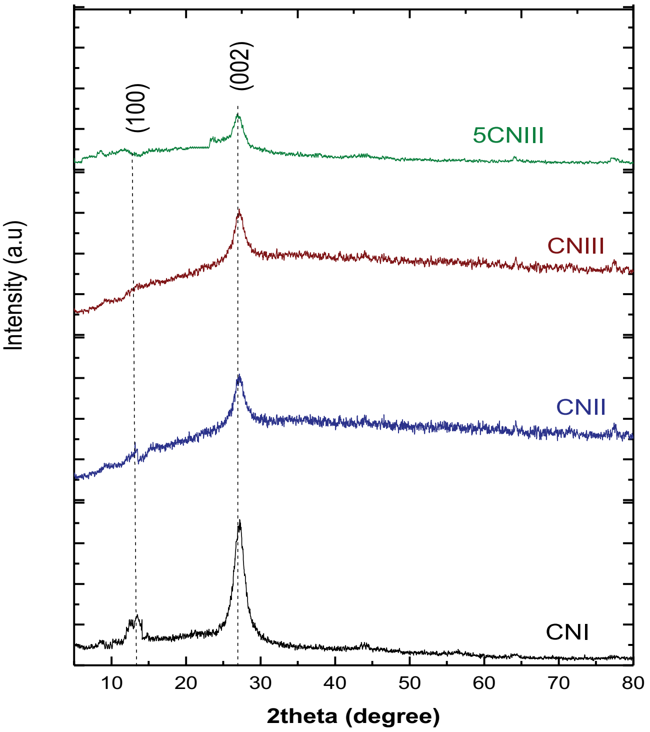

Fig. 1. Wide range XRD pattern for CNI, CNII, CNIII, and 5CNIII samples.

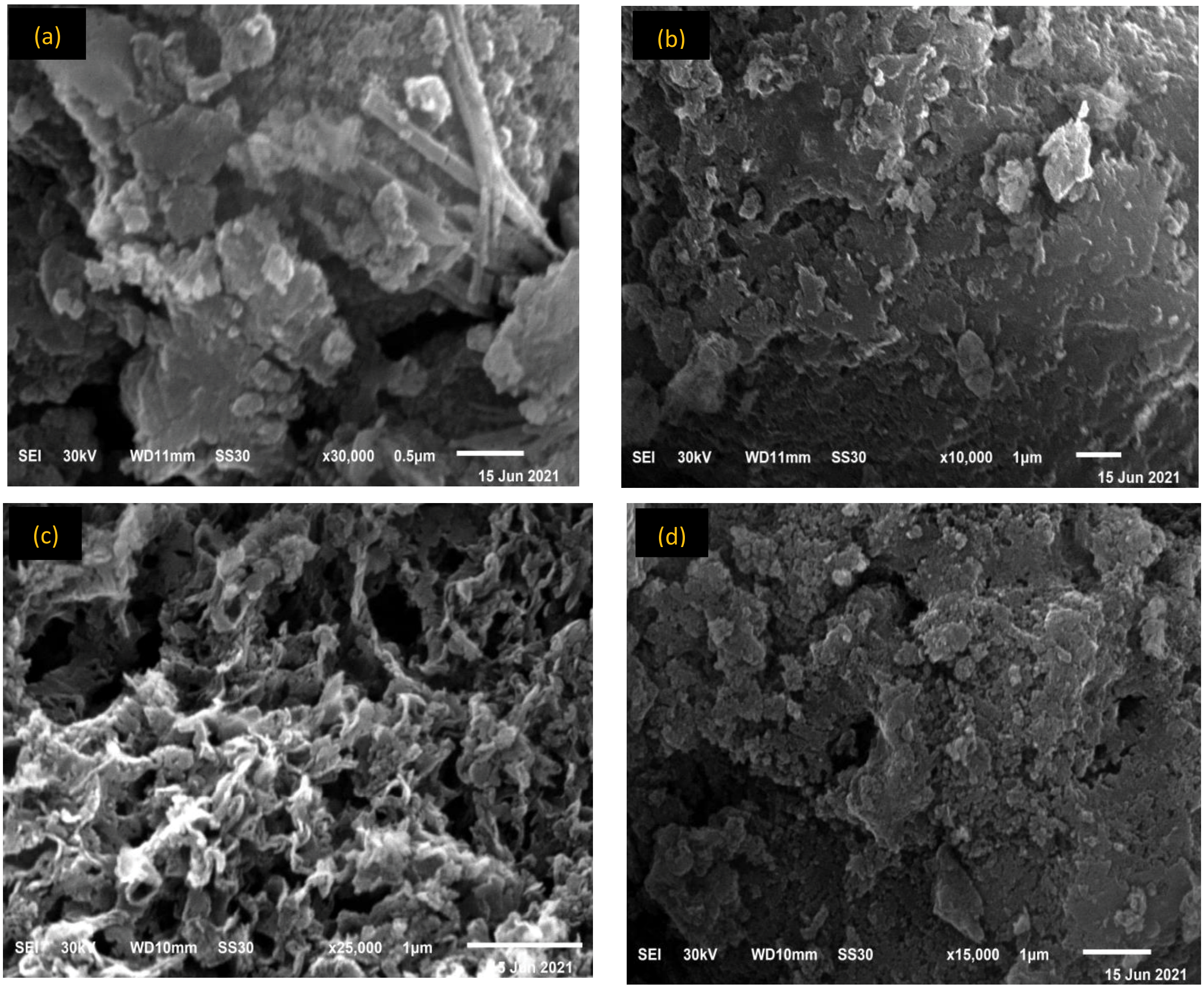

Fig. 2. (a–d) SEM images of CNI, CNII, CNIII, and 5CNIII, respectively.

The SEM images of CNI is shown in Fig. 2a which is composed of large agglomerates with some tubular without porous structures. The SEM images of CNII sample (Fig. 2b) contains both irregularly spherical particles and nanosheet morphologies. The SEM images of CNIII sample (Fig. 2c) exhibit a typical porous morphology with tubular structure. The surface morphology of 5CNIII sample shows small spherical Cu_2O particles dispersed homogeneously into the g-C_3N_4 nanosheets.

The chemical structures of CNI, CNII, and CNIII samples were examined by FT-IR technique (Fig. 3). As seen from this figure, the three samples display a broad band within the range 3,000–3,500 cm^{-1} which is assigned to the presence of N-H stretching vibration of uncondensed amine groups and/or O–H stretching vibration of physically adsorbed water molecules [22,42]. In addition, several bands in the range from 1,250–1,640 cm^{-1} corresponding to the characteristic stretching modes of heterocycles were also observed in the spectra. The band located at around 810 cm^{-1} is attributed to the breathing mode of triazine units [42,43].

For subject of comparison, Fig. 3 also illustrates the FT-IR spectra of 5CNIII sample. As indicated from this figure, an additional band at 625 cm^{-1} was detected, this absorption band originates from the stretching vibration of Cu–O bond [44,45]. This result confirms that Cu_2O particles successfully dispersed through CNIII sample to form a binary nanocomposite.

The textural properties of the tested samples were estimated from N_2 adsorption–desorption measurements at 77 K. Fig. 4 shows N_2 adsorption–desorption isotherms and pore size distribution curves of some selected samples. As indicated from Fig. 4a, CNII and CNIII samples exhibit isotherms of type IV with hysteresis loops which are characterized for mesoporous materials, while that for bulk g-C_3N_4 (CNI) shows isotherm like type III. Fig. 4b shows the pore size distribution curves of these samples which are characterized by the presence of one maximum located at 12.5, 17.2 and 13.5 nm for CNII, CNIII, and 5CNIII samples, respectively indicating the mesoporous structure of the samples. The results presented in Table 1 reveal that the BET surface area and the porosity of the materials depends on the method of preparation. Bulk g-C_3N_4 (CNI) measured the lowest surface area (5.8 m^2/g) with less porosity (0.012 cm^3/g). When synthesized colloidal silica was used as a template, CNII sample measured surface area of 50.4 m^2/g with a pore volume of 0.12 cm^3/g, while CNIII sample synthesized via sol-gel/thermal condensation method measured the highest surface area and pore volume (85.2 and 0.16 cm^3/g). Loading CNIII with different amounts of Cu_2O led to appreciable changes in the textural properties thus a respective 17.37%, 45.8% and 64.5% decrease occurred, in the area of 2CNIII, 5CNIII and 7CNIII samples relative to the value measured for the metal free sample (CNIII), this decrease may be related to blocking or filling of some narrow pores present at the surface of CNIII sample by deposition of Cu_2O species

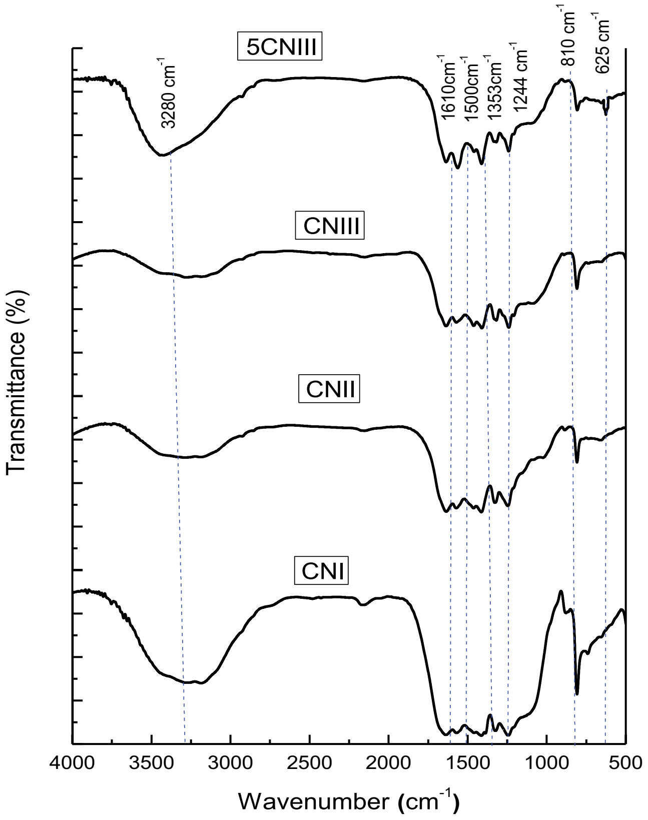

Fig. 3. FT-IR spectra of CNI, CNII, CNIII, and 5CNIII.

For further evaluation, the optical absorption of some tested samples was examined in the visible region (Fig. 5). The absorption edge for CNI, CNII, and CNIII samples were found to be 443, 468 and 480 nm, respectively, while that for 5CNIII sample was located at 510 nm. The band gap energy (E_g) of the samples were estimated based on the spectra obtained with UV-Vis and using Tauc equation [46] (Fig. 5b). E_g values for CNI, CNII, CNIII and 5CNIII were found to be 2.83, 2.74, 2.68, 2.41 eV, respectively. The above results indicate that loading of Cu_2O shifted the absorption edge of CNIII sample to a higher value thus decreasing it is band gap. The same behavior has been reported for many metal oxide/g-C_3N_4 composites and was related to the mixed effect of the quantum sized and the interface interactions between the two components in the composite [47,48].

Table 1
Texture properties of tested samples

Sample	S_{BET} (m^2/g)	V_p (CC/g)	Average crystal size (nm)
CNI	5.6	0.011	4.5
CNII	50.4	0.12	12.5
CNIII	85.2	0.16	17.2
1CNIII	81.4	0.146	16
2CNIII	70.4	0.139	14.5
5CNIII	46.2	0.0757	13.5
7CNIII	30.4	0.061	12.9

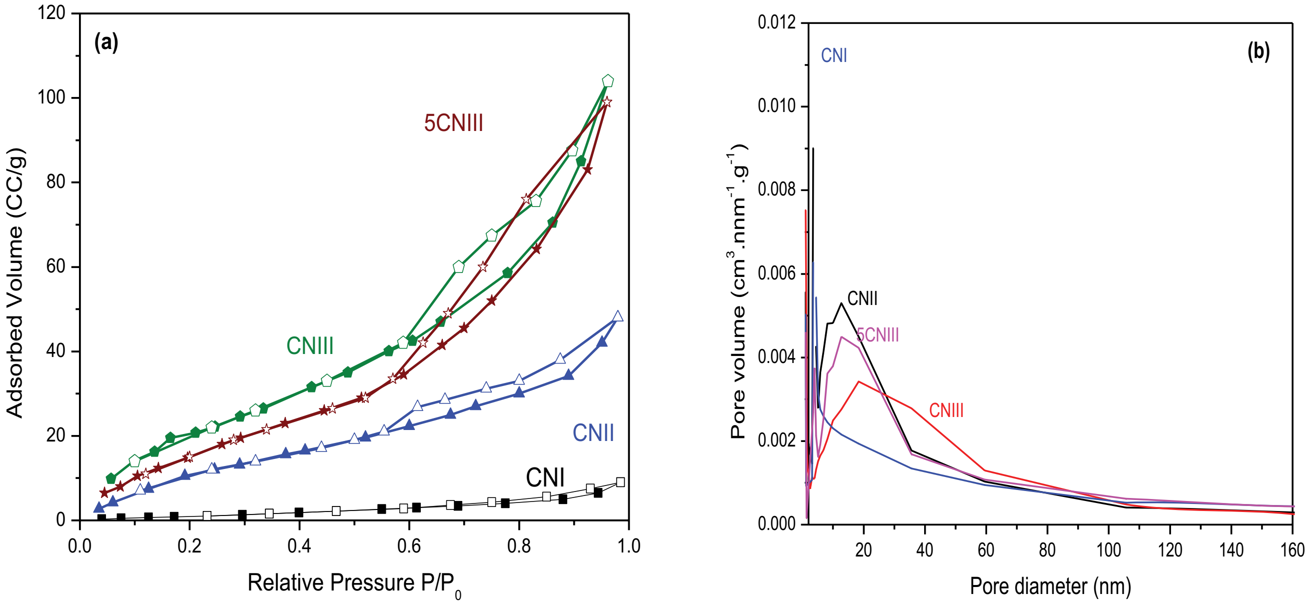

Fig. 4. (a) Nitrogen adsorption–desorption isotherms of some selected samples and (b) their corresponding pore size distribution.

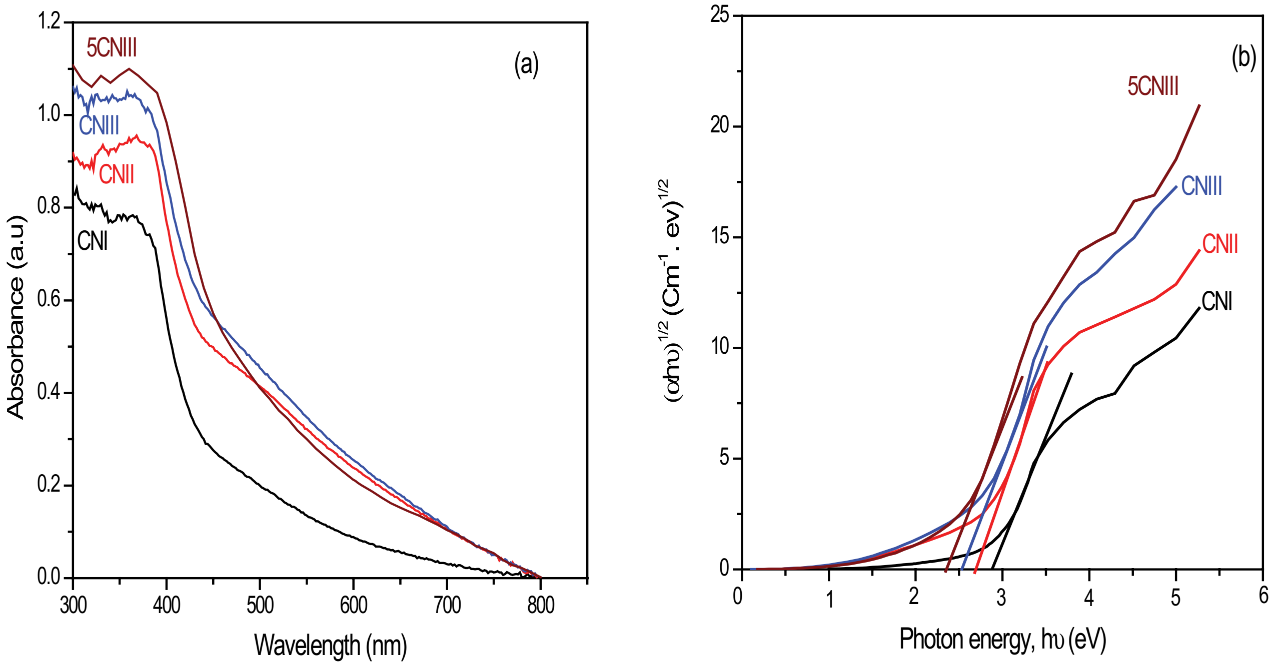

Fig. 5. (a) UV-Vis diffuse reflectance spectra of CNI, CNII, CNIII, and 5CNIII photocatalysts and (b) corresponding Tauc plots.

XPS analysis was also used to determine the composition and chemical state of the elements exit in CNIII and 5CNIII photocatalysts as representative samples. From the XPS survey spectrum of CNIII sample (Fig. 6a) two major signals corresponding to C and N with small one related to O can be easily observed. The C 1s spectra shown in Fig. 6b can be deconvoluted into three peaks at 288.27, 287.04 and 284.71 eV. The major C 1s peak centered at 288.27 eV is assigned to sp^2-bonded carbon (N–C=N) and the weaker one at 284.71 eV is related to sp^2 bonded carbon in C–C and usually observed on the XPS characterization for C_3N_4 materials [49,50].

The N 1s spectra Fig. 6c contains three peaks at 398.62, 400.54 and 404.57 eV. The main one is located at 398.62 eV and is related to sp^2 hybridized aromatic N in triazine rings [41] while the peak centered at 400.54 eV is attributed to tertiary nitrogen bonded to carbon atoms (N–$(C)_3$ and/or H–N–$(C)_2$) [45,51]. The minor peak at 404.57 eV is related to π excitations due to charging effects in heterocycles [51]. As mentioned before the XPS survey spectrum of CNIII sample contains a very weak signal corresponding to the presence of oxygen located at 532.19 eV, the presence of this signal with that measured for C 1s at 284.71 eV, may attributed the presence of C–O band, which could be formed as a result of adsorbed CO_2 [49].

The survey spectrum of 5CNIII (Fig. 7a) indicate the presence of C, O, N and Cu in the sample. The position of the binding energy peaks of C, O and N elements get slightly shifted toward lower value as result of loading CNIII sample with 5 wt.% Cu_2O. This indicates that the structure of CNIII is slightly altered by the addition of Cu_2O. For the Cu 2p spectrum (Fig. 7d), it displays six characteristics peaks. Cu $2p_{3/2}$ and Cu $2p_{1/2}$ of Cu^0 and/or Cu^{1+} were found as two main peaks at binding energies of 932.62 and 952.62 eV, respectively. The tiny peaks at 935.23, 944.14 and 955.6 eV could be attributed to the presence of Cu^{2+} species in the composite, which could be produced by the oxidation of Cu^0 and/or Cu^{1+} due to air and/or humidity exposure [45,52].

3.2. Photocatalytic degradation activity

The photocatalytic activity of the samples for degradation of RhB were carried out at 295 K and at natural PH values [7.0–6.8] under sunlight irradiation and illustrated in Fig. 8. A blank experiment in absence of photocatalyst showed that almost, no RhB photodegradation, indicating that the self-photolysis of RhB is negligible when irradiated with sunlight for 240 min. However, all photocatalysts show a considerable degradation activity in the presence of irradiation. The results indicated that 18.6%, 28.6%, 38.6% and 46.67% of RhB were photodegraded after 100 min irradiation for Cu_2O, CNI, CNII and CNIII samples. This data shows that the photodegradation activity of RhB without exception increased with increasing surface area and pore size of the photocatalyst. Materials with a high surface area and large pore size appear to have stronger photocatalytic activity [53]. For comparison, the performance of CNIII sample containing different amounts of Cu_2O was also included in Fig. 8. As noted from Fig. 8, the photocatalytic activity of CNIII for degradation of RhB was increased with increasing the amount Cu_2O loaded to reach 85.33% for 5CNIII. Upon further increasing of Cu_2O content from 5 to 7 wt.% the photocatalytic degradation activity of 7CNIII sample (not included in Fig. 8) remains almost constant. This may be taken as evidence that Cu_2O nanoparticles are photo-catalytically active sites and participate in the degradation of RhB. The area occupied by Cu_2O nanoparticles represent the active area for this process.

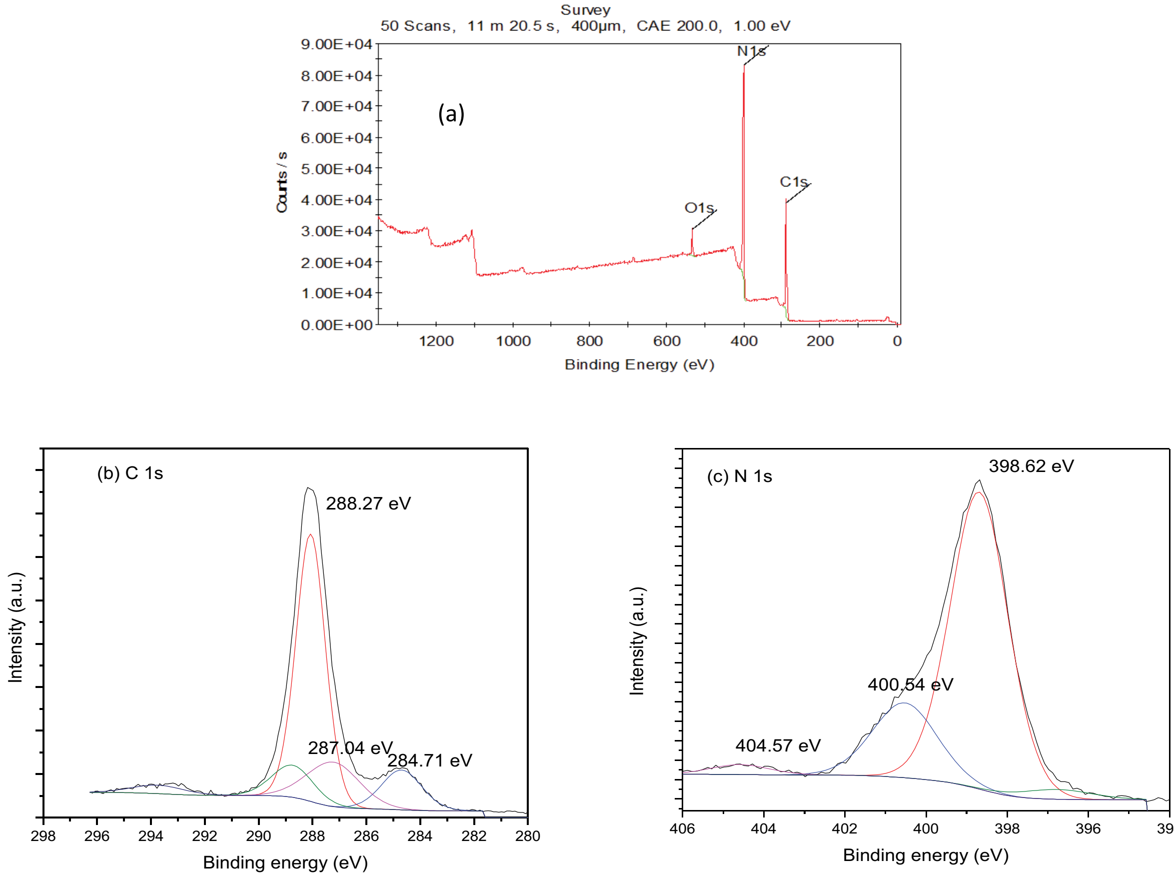

Fig. 6. (a) XPS survey spectral of CNIII sample and high-resolution XPS spectra of (b) C 1s peak, and (c) N 1s peak of CNIII sample.

Photocatalytic degradation of RhB over the photocatalysts was found to obey a pseudo-first-order equation at low concentration [54,55] according to the following equation:

$$\ln\left[\mathrm{RhB}\right]_t = \ln\left[\mathrm{RhB}\right]_0 - k_1 t \tag{1}$$

where $[\mathrm{RhB}]_0$ and $[\mathrm{RhB}]_t$ are concentrations of RhB dye at time of zero and t, respectively and k_1 is the pseudo-first-order kinetic constant. The kinetic results are given in Fig. 9, a good linearity of the data can be observed (R^2 = 0.97–0.99). The values of rate constant (k_1) as calculated from the slopes of these lines for Cu_2O, CNI, CNII and CNIII are 12.0×10^{-4}, 31.4×10^{-4}, 50.2×10^{-4} and 60.0×10^{-4} min^{-1}, respectively. By loading CNIII with Cu_2O the degradation kinetic constant considerably increases. K values of RhB degradation over 1CNIII, 2CNIII, and 5CNIII and 7CNIII samples are 10.5×10^{-3}, 14.6×10^{-3}, 18.4×10^{-3} and 18.0×10^{-3} min^{-1}, respectively. The sample containing 5 wt.% Cu_2O (5CNIII) exhibits the enhanced kinetic constant which is three times more than that of CNIII. As well-known Cu_2O photocatalyst can adsorb a light in the visible range which enhance the light absorption capacity of the samples. Furthermore, Cu_2O has a strong tendency to adsorb molecular oxygen which facilitate the scavenging of photogenerated electrons and suppress the recombination of electron-hole pairs at the interface [44,55].

The stability and longevity of photocatalysts are well established to be essential variables in practical applications. For this reason, 5CNIII sample was reused four times under the same conditions. The sample was collected by centrifugation in each run, then rinsed with DI H_2O, then ethanol and dried at 140°C for 1 h. No remarkable change in photocatalytic activity was observed. The photocatalytic activity measured for the first run was 81.33% while that for the fourth run was found to be 77.3%. As a result, the 5CNIII photocatalyst showed good photostability and can be used for practical applications.

Radical trapping tests have been carried out to estimate the role of reactive species in the RhB dye degradation activity. Fig. 10 shows the degradation efficiency of CNIII in absence and the presence of P-benzoquinone (BQ) scavenger of $O_2^{\bullet-}$, isopropyl alcohol (IPA) scavenger of $OH^{\bullet}$, silver nitrate ($AgNO_3$) scavenger of electrons, and potassium iodide (KI) scavenger of holes [17,18]. As can be noted from Fig. 10 that the degradation efficiency of CNIII photocatalyst in absence of any scavenger decreased from 81.33% to 44.2%, 34.7%, 65%, and 78.5% in the presence of BQ, KI, 2-IPA, $AgNO_3$, respectively. These results indicate that RhB degradation mainly is governed by superoxide radicals and photogenerated holes. Which means that two species play a significant role in the degradation of RhB over the tested photocatalysts.

Based on the above results the photocatalytic degradation of RhB over Cu_2O@CNIII photocatalysts can be described by the following scheme:

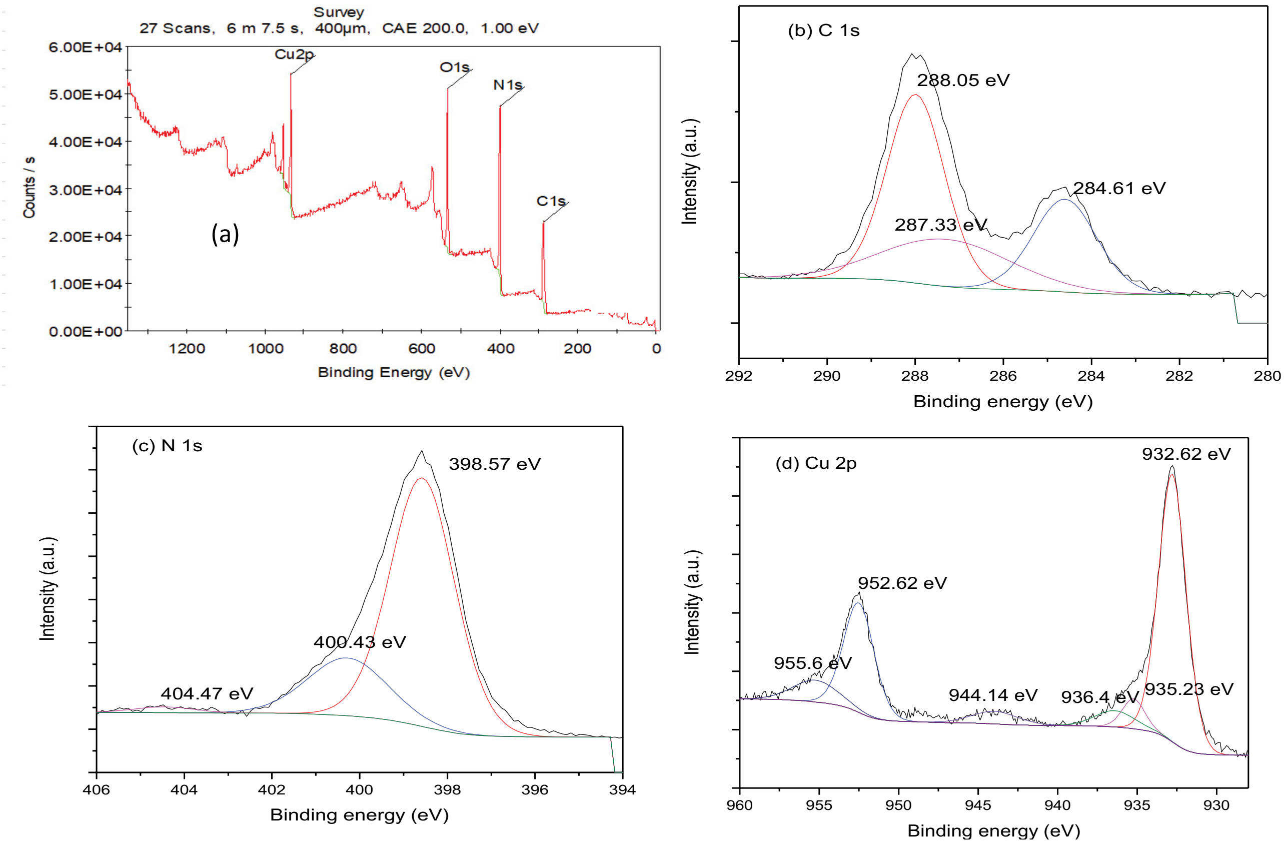

Fig. 7. (a) XPS survey spectral of 5CNIII sample and high-resolution XPS spectra of (b) C 1s peak, (c) N 1s peak, and (d) Cu 2p peak of 5CNIII sample.

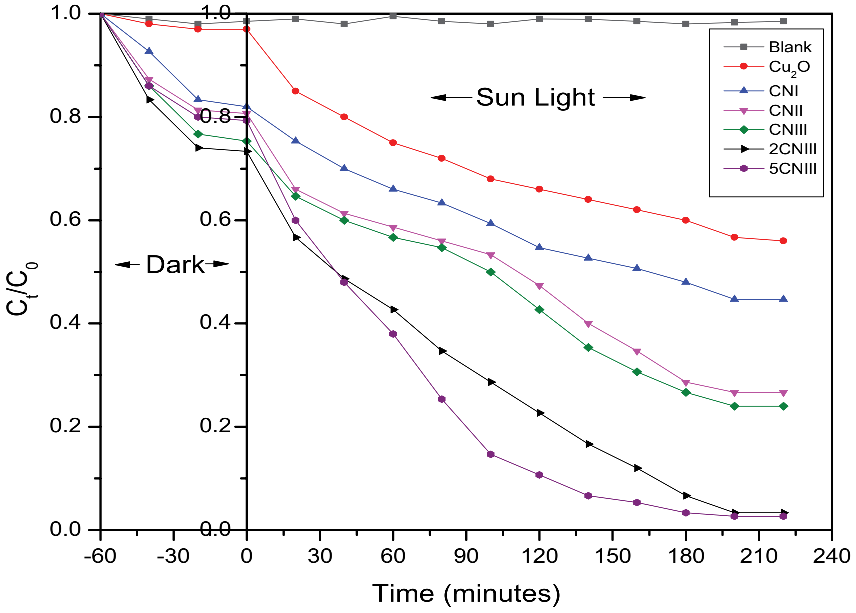

Fig. 8. Adsorption degradation profile of RhB over some selected samples.

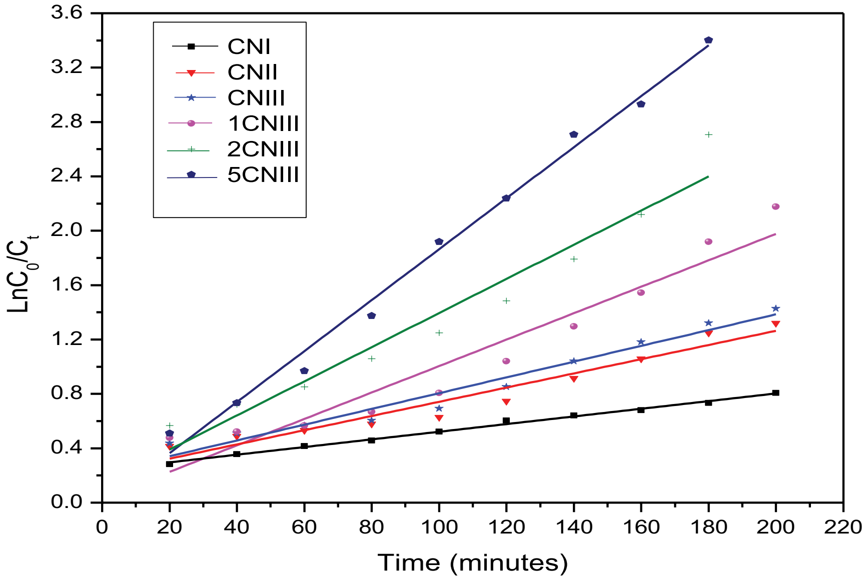

Fig. 9. Pseudo-first-order kinetic plots of some selected samples (Experimental conditions: $C_0 = 15$ ppm, Temp. = 25°C, dosage = 1.5 g/L, pH = 7).

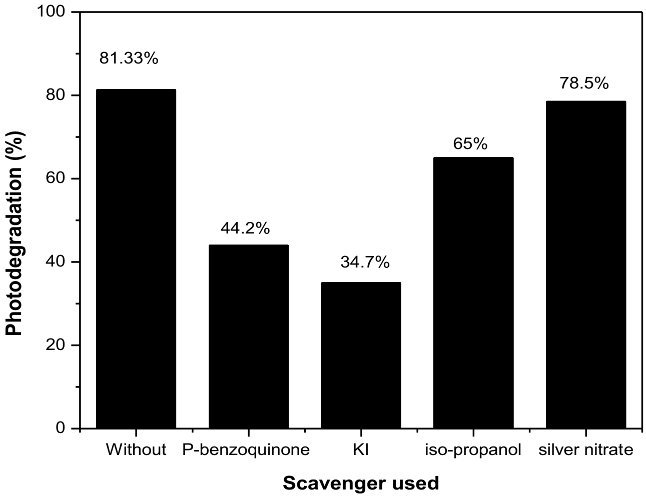

Fig. 10. Photodegradation activity of RhB over CNIII photocatalyst in the presence of various scavengers.

$$g\text{-}C_3N_4/Cu_2O + h\upsilon \rightarrow \frac{g\text{-}C_3N_4\left(h^+_{(VB)}\cdots e^-_{(CB)}\right)}{Cu_2O\left(h^+_{(VB)}\cdots e^-_{(CB)}\right)} \tag{1}$$

$$\frac{g\text{-}C_3N_4\left(h^+_{(VB)}\cdots e^-_{(CB)}\right)}{Cu_2O\left(h^+_{(VB)}\cdots e^-_{(CB)}\right)} \rightarrow g\text{-}C_3N_4\left(e^-\right) + Cu_2O\left(h^+\right) \tag{2}$$

$$Cu_2O\left(h^+\right) + H_2O \rightarrow Cu_2O + H^+ + OH^{\bullet} \tag{3}$$

$$Cu_2O\left(h^+\right) + OH^- \rightarrow Cu_2O + OH^{\bullet} \tag{4}$$

$$g\text{-}C_3N_4\left(e^-\right) + O_2 \rightarrow {}^{\bullet}O_2^- + g\text{-}C_3N_4 \tag{5}$$

$$RhB + h^+ \rightarrow \text{Degraded products}\left(\text{Major}\right) \tag{6}$$

$$RhB + {}^{\bullet}O_2^- \rightarrow \text{Degraded products}\left(\text{Major}\right) \tag{7}$$

$$RhB + OH^{\bullet} \rightarrow \text{Degraded products}\left(\text{Minor}\right) \tag{8}$$

As mentioned before the calculated bandgaps of CNIII and Cu_2O are 2.68 and 2.01 eV, respectively which means that both CNIII and Cu_2O can absorb photons and generate e^-–h^+ pairs under sunlight irradiation. So based on the energy band structure, both the conduction band (CB) and valence band (VB) of g-C_3N_4 are lower than those of Cu_2O [56], the excited state electrons of Cu_2O migrate directly to the CB of the g-C_3N_4 while the exited holes of g-C_3N_4 tend to transfer to the VB of Cu_2O. Trapped electrons at CB of g-C_3N_4 reduced molecular oxygen dissolved in the solution to produce reactive $^{\bullet}O_2^-$ and then h^+ and $^{\bullet}O_2^-$ are able directly to oxidize RhB dye due to their high oxidative capacity.

4. Conclusion

Rhodamine B dye (an organic pollutant) is efficiency degraded over metal free-porous g-C_3N_4 as well as on Cu_2O@g-C_3N_4 nanocomposites aqueous dispersion under irradiation by solar light. The photocatalytic activity of the porous g-C_3N_4 prepared by the sol-gel approach (CNIII) is higher than those measured for bulk (CNI) and even porous g-C_3N_4 prepared using synthesized colloidal silica template (CNII). Cu_2O@CNIII nanocomposites showed considerable enhancement in the photocatalytic degradation of RhB compared to the other metal-free g-C_3N_4 photocatalysts. The enhanced activity was attributed to the synergetic effect of both surface area and Cu_2O nanoparticles which provides more active sites for the degradation of RhB. The degradation data follow pseudo-first-order kinetic model. Superoxide radicals and photoinduced holes represent the main active species as recognized from radical trapping experiments. Finally, the photocatalysts under investigation showed an excellent photostability and can be reused up to four consecutive runs.

References

[1] S. Vigneshwaran, P. Sirajudheen, P. Karthikeyan, S. Meenakshi, Fabrication of sulfur-doped biochar derived from tapioca peel waste with superior adsorption performance for the removal of Malachite green and Rhodamine B dyes, Surf. Interfaces, 23 (2021) 100920, doi: 10.1016/j.surfin.2020.100920.

[2] S. Asha, C. Hentry, M.R. Bindhu, A.M. Al-Mohaimeed, M.R. Abdel Gawwad, M.S. Elshikh, Improved photocatalytic activity for degradation of textile dyeing waste water and thiazine dyes using $PbWO_4$ nanoparticles synthesized by co-precipitation method, Environ. Res., 200 (2021) 111721, doi: 10.1016/j.envres.2021.111721.

[3] T. Cheng, H. Gao, G. Liu, Z. Pu, S. Wang, Z. Yi, X. Wu, H. Yang, Preparation of core-shell heterojunction photocatalysts by coating CdS nanoparticles onto $Bi_4Ti_3O_{12}$ hierarchical microspheres and their photocatalytic removal of organic pollutants and Cr(VI) ions, Colloids Surf., A, 633 (2022) 127918, doi: 10.1016/j.colsurfa.2021.127918.

[4] N. Ahmad, J. Anae, M.Z. Khan, S. Sabir, X.J. Yang, V.K. Thakur, P. Campo, F. Coulon, Visible light-conducting polymer nanocomposites as efficient photocatalysts for the treatment of organic pollutants in wastewater, J. Environ. Manage., 295 (2021) 113362, doi: 10.1016/j.jenvman.2021.113362.

[5] F.P. de Freitas, A.M.M.L. Carvalho, A. de C.O. Carneiro, M.A. de Magalhães, M.F. Xisto, W.D. Canal, Adsorption of neutral red dye by chitosan and activated carbon composite films, Heliyon, 7 (2021) e07629, doi: 10.1016/j.heliyon.2021.e07629.

[6] M. Vakili, P. Amouzgar, G. Cagnetta, B. Wang, X. Guo, A. Mojiri, E. Zeimaran, B. Salamatinia, Ultrasound-assisted preparation of chitosan/nano-activated carbon composite beads aminated with (3-aminopropyl)triethoxysilane for adsorption of acetaminophen from aqueous solutions, Polymers (Basel), 11 (2019) 1701, doi: 10.3390/polym11101701.

[7] F.I. El-Dossoki, T.M. Atwee, A.M. Hamada, A.A. El-Bindary, Photocatalytic degradation of Remazol Red B and Rhodamine B dyes using TiO_2 nanomaterial: estimation of the effective operating parameters, Desal. Water Treat., 233 (2021) 319–330.

[8] E.E. El-Katori, M.A. Ahmed, A.A. El-Bindary, A.M. Oraby, Impact of CdS/SnO_2 heterostructured nanoparticle as visible light active photocatalyst for the removal methylene blue dye, J. Photochem. Photobiol., A, 392 (2020) 112403, doi: 10.1016/j.jphotochem.2020.112403.

[9] O.B. Ayodele, O.S. Togunwa, Catalytic activity of copper modified bentonite supported ferrioxalate on the aqueous degradation and kinetics of mineralization of Direct Blue 71, Acid Green 25 and Reactive Blue 4 in photo-Fenton process, Appl. Catal., A, 470 (2014) 285–293.

[10] A.R. Binupriya, M. Sathishkumar, C.S. Ku, S.-I. Yun, Sequestration of Reactive Blue 4 by free and immobilized *Bacillus subtilis* cells and its extracellular polysaccharides, Colloids Surf., B, 76 (2010) 179–185.

[11] X. Jin, R. Wang, P. Jin, X. Shi, Y. Wang, L. Xu, X. Wang, H. Xu, How can accumulated organics and salts deteriorate the biological treatment unit in the printing and dyeing wastewater recycling system?, Chem. Eng. J., 413 (2021) 127528, doi: 10.1016/j.cej.2020.127528.

[12] A. Giwa, A. Dindi, J. Kujawa, Membrane bioreactors and electrochemical processes for treatment of wastewaters containing heavy metal ions, organics, micropollutants and dyes: recent developments, J. Hazard. Mater., 370 (2019) 172–195.

[13] M. Shirvani, L. Naji, Interface engineering of electrochemically deposited ZnO nanorods as electron transport layer in polymer solar cells using organic dyes, Mater. Chem. Phys., 259 (2021) 124064, doi: 10.1016/j.matchemphys.2020.124064.

[14] M. Sleiman, D. Vildozo, C. Ferronato, J.-M. Chvelon, Photocatalytic degradation of azo dye Metanil Yellow: optimization and kinetic modeling using a chemometric approach, Appl. Catal., B, 77 (2007) 1–11.

[15] J. Sun, X. Wang, J. Sun, R. Sun, S. Sun, L. Qiao, Photocatalytic degradation and kinetics of Orange G using nano-sized Sn(IV)/TiO_2/AC photocatalyst, J. Mol. Catal. A: Chem., 260 (2006) 241–246.

[16] T. Cheng, H. Gao, R. Li, S. Wang, Z. Yi, H. Yang, Flexoelectricity-induced enhancement in carrier separation and photocatalytic activity of a photocatalyst, Appl. Surf. Sci., 566 (2021) 150669, doi: 10.1016/j.apsusc.2021.150669.

[17] H.A. Kiwaan, T.M. Atwee, E.A. Azab, A.A. El-Bindary, Photocatalytic degradation of organic dyes in the presence of nanostructured titanium dioxide, J. Mol. Struct., 1200 (2020) 127115, doi: 10.1016/j.molstruc.2019.127115.

[18] H.A. Kiwaan, T.M. Atwee, E.A. Azab, A.A. El-Bindary, Efficient photocatalytic degradation of Acid Red 57 using synthesized ZnO nanowires, J. Chin. Chem. Soc., 66 (2019) 89–98.

[19] A. Di Paola, G. Cufalo, M. Addamo, M. Bellardita, R. Campostrini, M. Ischia, R. Ceccato, L. Palmisano, Photocatalytic activity of nanocrystalline TiO_2 (brookite, rutile and brookite-based) powders prepared by thermohydrolysis of $TiCl_4$ in aqueous chloride solutions, Colloids Surf., A, 317 (2008) 366–376.

[20] M. Ghorbanpour, S. Lotfiman, Solid-state immobilisation of titanium dioxide nanoparticles onto nanoclay, Micro Nano Lett., 11 (2016) 684–687.

[21] M. Ghorbanpour, C. Falamaki, Micro energy dispersive X-ray fluorescence as a powerful complementary technique for the analysis of bimetallic Au/Ag/glass nanolayer composites used in surface plasmon resonance sensors, Appl. Opt., 51 (2012) 7733–7738.

[22] M.B. Shekardasht, M.H. Givianrad, P. Gharbani, Z. Mirjafary, A. Mehrizad. Preparation of a novel Z-scheme g-C_3N_4/RGO/$Bi_2Fe_4O_9$ nanophotocatalyst for degradation of Congo red dye under visible light, Diamond Relat. Mater., 109 (2020) 108008, doi: 10.1016/j.diamond.2020.108008.

[23] M. Danish, M. Muneer, Facile synthesis of highly efficient Co@ZnSQDs/g-C_3N_4/MWCNT nanocomposites and their photocatalytic potential for the degradation of RhB dye: efficiency, degradation kinetics, and mechanism pathway, Ceram. Int., 47 (2021) 13043–13056.

[24] W. Shi, W. Sun, Y. Liu, X. Li, X. Lin, F. Guo, Y. Hong, Onion-ring-like g-C_3N_4 modified with Bi_3TaO_7 quantum dots: a novel 0D/3D S-scheme heterojunction for enhanced photocatalytic hydrogen production under visible light irradiation, Renewable Energy, 182 (2021) 958–968.

[25] G. Wang, Y. Zhao, H. Ma, C. Zhang, X. Dong, X. Zhang, Enhanced peroxymonosulfate activation on dual active sites of N vacancy modified g-C_3N_4 under visible-light assistance and its selective removal of organic pollutants, Sci. Total Environ., 756 (2021) 144139, doi: 10.1016/j.scitotenv.2020.144139.

[26] D. Liu, Z. Jin, H. Li, G. Lu, Modulation of the excited-electron recombination process by introduce g-C_3N_4 on Bi-based bimetallic oxides photocatalyst, Appl. Surf. Sci., 423 (2017) 255–265.

[27] P. Lu, X. Hu, Y. Li, Y. Peng, M. Zhang, X. Jiang, Y. He, M. Fu, F. Dong, Z. Zhang, Novel $CaCO_3$/g-C_3N_4 composites with enhanced charge separation and photocatalytic activity, J. Saudi Chem. Soc., 23 (2019) 1109–1118.

[28] P. Guo, F. Zhao, X. Hu, Boron-and europium-co-doped g-C_3N_4 nanosheets: enhanced photocatalytic activity and reaction mechanism for tetracycline degradation, Ceram. Int., 47 (2021) 16256–16268.

[29] W. Li, X. Chu, F. Wang, Y. Dang, X. Liu, X. Wang, C. Wang, Enhanced cocatalyst-support interaction and promoted electron transfer of 3D porous g-C_3N_4/GO-M (Au, Pd, Pt) composite catalysts for hydrogen evolution, Appl. Catal., B, 288 (2021) 120034, doi: 10.1016/j.apcatb.2021.120034.

[30] T. Tong, B. Zhu, C. Jiang, B. Cheng, J. Yu, Mechanistic insight into the enhanced photocatalytic activity of single-atom Pt, Pd or Au-embedded g-C_3N_4, Appl. Surf. Sci., 433 (2018) 1175–1183.

[31] Y. Liu, H. Zhang, Y. Jiang, A new noble-metal-free co-catalyst V_8C_7 on g-C_3N_4 with enhanced photocatalytic H_2 evolution activity, Appl. Catal., A, 625 (2021) 118341, doi: 10.1016/j.apcata.2021.118341.

[32] A.A. El-Bindary, S.M. El-Marsafy, A.A. El-Maddah, Enhancement of the photocatalytic activity of ZnO nanoparticles by silver doping for the degradation of AY99 contaminants, J. Mol. Struct., 1191 (2019) 76–84.

[33] M.A. Karimi, M. Atashkadi, M. Ranjbar, A. Habibi-Yangjeh, Novel visible-light-driven photocatalyst of NiO/Cd/g-C_3N_4 for enhanced degradation of methylene blue, Arabian J. Chem., 13 (2020) 5810–5820.

[34] G.R. Surikanti, P. Bajaj, M.V. Sunkara, g-C_3N_4-mediated synthesis of Cu_2O To obtain porous composites with improved visible light photocatalytic degradation of organic dyes, ACS Omega, 4 (2019) 17301–17316.

[35] R. Mohammadi, B. Gholipour, H. Alamgholiloo, S. Rostamnia, H. Mohtasham, A. Zonouzi, S. Ramakrishna, M. Shokouhimehr, Nano-construction of CuO nanorods decorated with g-C_3N_4 nanosheets (CuO/g-C_3N_4-NS) as a superb colloidal nanocatalyst for liquid phase C–H conversion of aldehydes to amides, J. Mol. Liq., 334 (2021) 116063, doi: 10.1016/j.molliq.2021.116063.

[36] V.S. Manikandan, S. Harish, J. Archana, M. Navaneethan, Fabrication of novel hybrid Z-Scheme WO_3@g-C_3N_4@MWCNT nanostructure for photocatalytic degradation of tetracycline and the evaluation of antimicrobial activity, Chemosphere, 287 (2022) 132050, doi: 10.1016/j.chemosphere.2021.132050.

[37] K. Moeller, J. Kobler, T. Bein, Colloidal suspensions of nanometer-sized mesoporous silica, Adv. Funct. Mater., 17 (2007) 605–612.

[38] K. Kailasam, J.D. Epping, A. Thomas, S. Losse, H. Junge, Mesoporous carbon nitride–silica composites by a combined sol–gel/thermal condensation approach and their application as photocatalysts, Energy Environ. Sci., 4 (2011) 4668–4674.

[39] D.P. Lapham, J.L. Lapham, BET surface area measurement of commercial magnesium stearate by krypton adsorption in preference to nitrogen adsorption, Int. J. Pharm., 568 (2019) 118522, doi: 10.1016/j.ijpharm.2019.118522.

[40] P. Peng, H. Han, L. Hu, C. Guo, Y. Gao, Y. Xie, The calculations of pore structure parameters from gas adsorption experiments of shales: which models are better?, J. Nat. Gas Sci. Eng., 94 (2021) 104060, doi: 10.1016/j.jngse.2021.104060.

[41] H. Zhang, T. Ouyang, J. Li, M. Mu, X. Yin, Dual 2D CuSe/g-C_3N_4 heterostructure for boosting electrocatalytic reduction of CO_2, Electrochim. Acta, 390 (2021) 138766, doi: 10.1016/j.electacta.2021.138766.

[42] N. Farooq, A. ur Rehman, A.M. Qureshi, Z. Ur Rehman, A. Ahmad, M.K. Aslam, H.M.A. Javed, S. Hussain, M.A. Habila, N. Al Masoud, T. Saad Alomar, Au@GO@g-C_3N_4 and Fe_2O_3 nanocomposite for efficient photocatalytic and electrochemical applications, Surf. Interfaces, 26 (2021) 101399, doi: 10.1016/j.surfin.2021.101399.

[43] N. Hussain, H. Alawadhi, S.M.A. Rahman, M.A. Abdelkareem, Facile synthesis of novel Cu_2O-g-C_3N_4/Vulcan carbon composite as anode material with enhanced electrochemical performances in urea fuel cell, Sustainable Energy Technol. Assess., 45 (2021) 101107, doi: 10.1016/j.seta.2021.101107.

[44] A.M. Paul, A. Sajeev, R. Nivetha, K. Gothandapani, P. Bhardwaj, K. Govardhan, V. Raghavan, G. Jacob, R. Sellapan, S.K. Jeong, A.N. Grace, Cuprous oxide (Cu_2O)/graphitic carbon nitride (g-C_3N_4) nanocomposites for electrocatalytic hydrogen evolution reaction, Diamond Relat. Mater., 107 (2020) 107899, doi: 10.1016/j.diamond.2020.107899.

[45] D. Li, S. Zuo, H. Xu, J. Zan, L. Sun, D. Han, W. Liao, B. Zhang, D. Xia, Synthesis of a g-C_3N_4-Cu_2O heterojunction with enhanced visible light photocatalytic activity by PEG, J. Colloid Interface Sci., 531 (2018) 28–36.

[46] L. Jarosiński, J. Pawlak, S.K.J. Al-Ani, Inverse logarithmic derivative method for determining the energy gap and the type of electron transitions as an alternative to the Tauc method, Opt. Mater., 88 (2019) 667–673.

[47] Z. Yang, D. Chu, G. Jia, M. Yao, B. Liu, Significantly narrowed bandgap and enhanced charge separation in porous, nitrogen-vacancy red g-C_3N_4 for visible light photocatalytic H_2 production, Appl. Surf. Sci., 504 (2020) 144407, doi: 10.1016/j.apsusc.2019.144407.

[48] C. Ji, S. Yin, S. Sun, S. Yang, An in situ mediator-free route to fabricate Cu_2O/g-C_3N_4 type-II heterojunctions for enhanced visible-light photocatalytic H_2 generation, Appl. Surf. Sci., 434 (2018) 1224–1231.

[49] G.X. Zhu, T.L. Lu, L. Han, Y.Z. Zhan, Graphitic carbon nitride (g-C_3N_4) as an efficient metal-free Fenton-like catalyst for degrading organic pollutants: the overlooked non-photocatalytic activity, Water Sci. Technol., 81 (2020) 518–528.

[50] I. Ahmad, Comparative study of metal (Al, Mg, Ni, Cu and Ag) doped ZnO/g-C_3N_4 composites: efficient photocatalysts for the degradation of organic pollutants, Sep. Purif. Technol., 251 (2020) 117372, doi: 10.1016/j.seppur.2020.117372.

[51] L. He, M. Fei, J. Chen, Y. Tian, Y. Jiang, Y. Huang, K. Xu, J. Hu, Z. Zhao, Q. Zhang, H. Ni, L. Chen, Dataset of emission and excitation spectra, UV–vis absorption spectra, and XPS spectra of graphitic C_3N_4, Data Brief, 21 (2018) 501–510.

[52] T. Zhang, I.P. Souza, J. Xu, V.C. Almeida, T. Asefa, Mesoporous graphitic carbon nitrides decorated with Cu nanoparticles: efficient photocatalysts for degradation of tartrazine yellow dye, Nanomaterials (Basel), 8 (2018) 636, doi: 10.3390/nano8090636.

[53] X. Ye, S. Shi, Y. Zeng, M. Ding Z. Wu, Carbon defective carbon nitride with large specific surface area by hot oxygen etching for promoting photocatalytic performance, Colloids Surf., A, 632 (2022) 127732, doi: 10.1016/j.colsurfa.2021.127732.

[54] A.T. Dhiwahar, S. Maruthamuthu, R. Marnadu, M. Sundararajan, M. Aslam Manthrammel, M. Shkir, P. Sakthivel, V.R.M. Reddy, Improved photocatalytic degradation of Rhodamine B under visible light and magnetic properties using microwave combustion grown Ni doped copper ferrite spinel nanoparticles, Solid State Sci., 113 (2021) 106542, doi: 10.1016/j.solidstatesciences.2021.106542.

[55] C. Zhou, Z. Liu, L. Fang, Y. Guo, Y. Feng, M. Yang, Kinetic and mechanistic study of Rhodamine B degradation by H_2O_2 and Cu/Al_2O_3/g-C_3N_4 composite, Catalysts, 10 (2020) 317, doi: 10.3390/catal10030317.

[56] H. Yang, A short review on heterojunction photocatalysts: carrier transfer behavior and photocatalytic mechanisms, Mater. Res. Bull., 142 (2021) 111406, doi: 10.1016/j.materresboll.2021.111406.